HH 666: Different kinematics from Hα and [Fe II] emission provide a missing link between jets and outflows

Megan Reiter[1]⋆, Nathan Smith[1], Megan M. Kiminki[1], and John Bally[2]
[1]*Steward Observatory, University of Arizona, Tucson, 933 N. Cherry Ave, Tucson, AZ 85721, USA*
[2]*Center for Astrophysics and Space Astronomy, University of Colorado, 389 UCB, Boulder, CO 80309, USA*

ABSTRACT
HH 666 is an externally irradiated protostellar outflow in the Carina nebula for which we present new near-IR [Fe II] spectra obtained with the FIRE spectrograph at Magellan Observatory. Earlier Hα and near-IR [Fe II] imaging revealed that the two emission lines trace substantially different morphologies in the inner $\sim 40''$ of the outflow. Hα traces a broad cocoon that surrounds the collimated [Fe II] jet that extends throughout the parent dust pillar. New spectra show that this discrepancy extends to their kinematics. Near-IR [Fe II] emission traces steady, fast velocities of ± 200 km s^{-1} from the eastern and western limbs of the jet. We compare this to a previously published Hα spectrum that reveals a Hubble-flow velocity structure near the jet-driving source. New, second-epoch *HST*/ACS Hα images reveal the *lateral* spreading of the Hα outflow lobe away from the jet axis. Hα proper motions also indicate a sudden increase in the mass-loss rate ~ 1000 yr ago, while steady [Fe II] emission throughout the inner jet suggest that the burst is ongoing. An accretion burst sustained for ~ 1000 yr is an order of magnitude longer than expected for FU Orionis outbursts, but represents only a small fraction of the total age of the HH 666 outflow. Altogether, available data suggests that [Fe II] traces the highly collimated protostellar *jet* while Hα traces the entrained and irradiated *outflow*. HH 666 appears to be a missing link between bare jets seen in H II regions and entrained molecular outflows seen from embedded protostars in more quiescent regions.

Key words: stars: formation — jets — outflows

1 INTRODUCTION

Over a wide range of initial masses, stars appear to drive an outflow at some stage in their formation. Mounting evidence calls into question whether there is an upper limit on the mass of protostars that may drive collimated jets, despite uncertainty about whether the dominant physics of formation may change between low and high masses (e.g. Garay et al. 2003; Caratti o Garatti et al. 2008; Guzmán et al. 2012; Duarte-Cabral et al. 2013; Reiter & Smith 2013). These jets will interact with and shape – and be shaped by – the circumstellar molecular envelope and larger natal cloud. Various jet properties and morphologies, such as asymmetries (e.g. Reipurth et al. 1998; Bally & Reipurth 2001), wiggles and gaps (e.g. De Gouveia et al. 1996), the degree of collimation (Mundt et al. 1991), and decreasing knot velocities have been explained by interaction with different kinds of environments.

Interaction between the protostellar jet and ambient gas in the star forming cloud has been proposed as a mechanism to create molecular outflows. Raga & Cabrit (1993) offer a simple analytical model wherein molecular outflows are the product of environmental gas being entrained by a protostellar jet. While some molecular outflows are well-described by jet-entrainment (see, e.g. Zinnecker et al. 1998; Arce & Sargent 2005, 2006), others show a conical morphology and broader range of velocities in the outflowing gas that have been interpreted as a wide-angle wind launched from the protostellar disc (e.g. Nagar et al. 1997; Klaassen et al. 2013; Salyk et al. 2014). A full evolutionary scenario may involve a combination of these two, with different components dominating at different times (e.g. Shang et al. 2006; Zapata et al. 2014). In either case, the outflow will clear material along the jet axis, creating a polar cavity as it travels through the protostellar envelope and into the surrounding molecular cloud. Clearing of the protostellar envelope may explain the apparent widening of molecular outflows associated with more evolved sources (Arce & Sargent 2006).

In the unobscured environment outside the natal cloud,

⋆ E-mail: mreiter@as.arizona.edu (MR)

Table 1. Observations

Instrument	Filter / Position	Date	Int. time	Comment	Ref.
ACS/*HST*	F658N	2005 Mar 30	1000 s	Hα + [N II]	Smith et al. (2010)
ACS/*HST*	F658N	2014 Feb 21	1000 s	Hα + [N II]	this work
WFC3-UVIS/*HST*	F656N	2009 Jul 24	7920 s	Hα	Reiter & Smith (2013)
WFC3-UVIS/*HST*	F673N	2009 Jul 24	9600 s	[S II] $\lambda6717 + \lambda6731$	Reiter & Smith (2013)
WFC3-IR/*HST*	F126N	2009 Jul 25	600 s	[Fe II] $\lambda12567$	Reiter & Smith (2013)
WFC3-IR/*HST*	F164N	2009 Jul 25	700 s	[Fe II] $\lambda16435$	Reiter & Smith (2013)
EMMI/*NTT*	Hα	2003 Mar 11	2400 s	P.A. = 293.5°	Smith et al. (2004)
FIRE/*Magellan*	HH 666 M	2013 Feb 22	600 s	P.A. = 110°	this work
FIRE/*Magellan*	HH 666 IRS	2013 Feb 22	600 s	P.A. = 110°	this work
FIRE/*Magellan*	HH 666 O	2013 Feb 22	600 s	P.A. = 115°	this work

optical and near-IR emission lines can be used as a tracer of the protostellar *jet* (e.g. Sepúlveda et al. 2011). Longer wavelength emission lines from shock-excited molecules, on the other hand, sample embedded parts of the entrained *outflow* propagating within a molecular cloud (e.g. Noriega-Crespo et al. 2004). In this paper, we refer to the *jet* as the fast, highly collimated stream of gas launched near the poles of the protostar and the *outflow* as the slower, wide-angle component of outflowing gas that either originated in the protostellar disc, or in the ambient medium that was entrained by shocks in the passing jet. Outflows tend to be observed in more embedded regions (e.g. Beltrán et al. 2008; Beuther et al. 2008; Forbrich et al. 2009; Fuente et al. 2009; Takahaski & Ho 2012). The underlying collimated jets are primarily atomic and remain invisible unless excited by shocks or external irradiation. For both excitation mechanisms, bare jets emerging from more evolved, unembedded sources will emit at visual and UV wavelengths (e.g. Reipurth et al. 1998; Bally & Reipurth 2001; McGroarty et al. 2004). Observing both the jet and the outflow in a single source is difficult, but understanding how the jet interacts with the surrounding cloud is important for constraining local momentum feedback. Partially embedded jets offer one way to bridge these two regimes. For example, a protostar residing near the edge of a cloud or in a small, isolated globule may drive a jet into the relatively diffuse environment outside the cloud. At the same time, the counter-jet plows deeper into the molecular cloud where its presence must be inferred from the shape of the outflow lobe it creates. Jets and outflow lobes have been seen to coexist in several protostellar sources (e.g. HH 111: Nagar et al. 1997; LeFloch et al. 2007; HH 46/47: Noriega-Crespo et al. 2004; Arce et al. 2013; and HH 300: Reipurth et al. 2000; Arce & Goodman 2001a).

In the Carina nebula, HH 666 emerges from a translucent pillar into a giant H II region created by more than ~ 65 O-type stars (see Smith 2006a). Smith et al. (2004) discovered the outflow in ground-based narrowband optical images and identified several large knots that extend more than 4 pc on the sky (features HH 666 D, A, E, M, O, N, I, and C). The mass-loss rates (Smith et al. 2010; Reiter & Smith 2013) and outflow velocities (Reiter & Smith 2014) measured in HH 666 are among the highest of the jets in Carina, making it one of the most powerful jets known (see, e.g. Figure 14 in Ellerbroek et al. 2013). Harsh UV radiation from the many massive stars in Carina permeates the region, il-

luminating the dust pillar from which HH 666 emerges and irradiating the body of the jet itself. External irradiation lights up neutral material in the jet that is not excited in shocks, revealing portions of the jet that would otherwise remain invisible. This allows the physical properties of the jet to be derived using the diagnostics of photoionized gas (e.g. Bally et al. 2006; Smith et al. 2010). However, massive star feedback illuminates indiscriminately, irradiating both the jet and the surrounding environment, which can complicate the interpretation of the observed emission. Non-uniform density structures in a photoionized jet can further complicate the interpretation. Fortunately, multi-wavelength observations allow us to disentangle the jet from its complex environment.

Smith et al. (2004) and Reiter & Smith (2013) showed that near-IR [Fe II] emission from HH 666 traces the jet inside the $\sim 40''$ wide pillar, connecting the large-scale jet seen in Hα to the IR-bright protostar that drives it (HH 666 IRS). High angular resolution near-IR narrowband [Fe II] images obtained with Wide-Field Camera 3 (WFC3-IR) on the *Hubble Space Telescope (HST)* reveal additional morphological complexities (see Figure 1 and Reiter & Smith 2013). Near the driving source, [Fe II] emission traces portions of the jet that are not seen in Hα. In the western limb of the inner jet, designated HH 666 M, [Fe II] emission bisects a dark cavity to the northwest of HH 666 IRS, clearly connecting the jet to its driving source. [Fe II] emission from HH 666 O, the eastern limb of the inner jet, traces a collimated jet body that appears to be surrounded by a broad cocoon of Hα emission. Curiously, Smith et al. (2004) see a Hubble-like velocity structure in Hα and [S II] spectra of the inner parts of HH 666 (features HH 666 M and O). Only two other protostellar jets have shown Hubble-like velocity structures in optical spectra (HH 83, Reipurth et al. 1989; and HH 900, Reiter et al. 2015).

In this paper, we present new ground-based near-IR [Fe II] spectroscopy and a second epoch of *HST*/ACS Hα images. When combined with extant data, the *HST* images allow us to compare the kinematics of these two morphologically distinct components. Together, these new data offer a self-consistent explanation for the curious morphological and kinematic differences between the Hα and [Fe II] emission from HH 666.
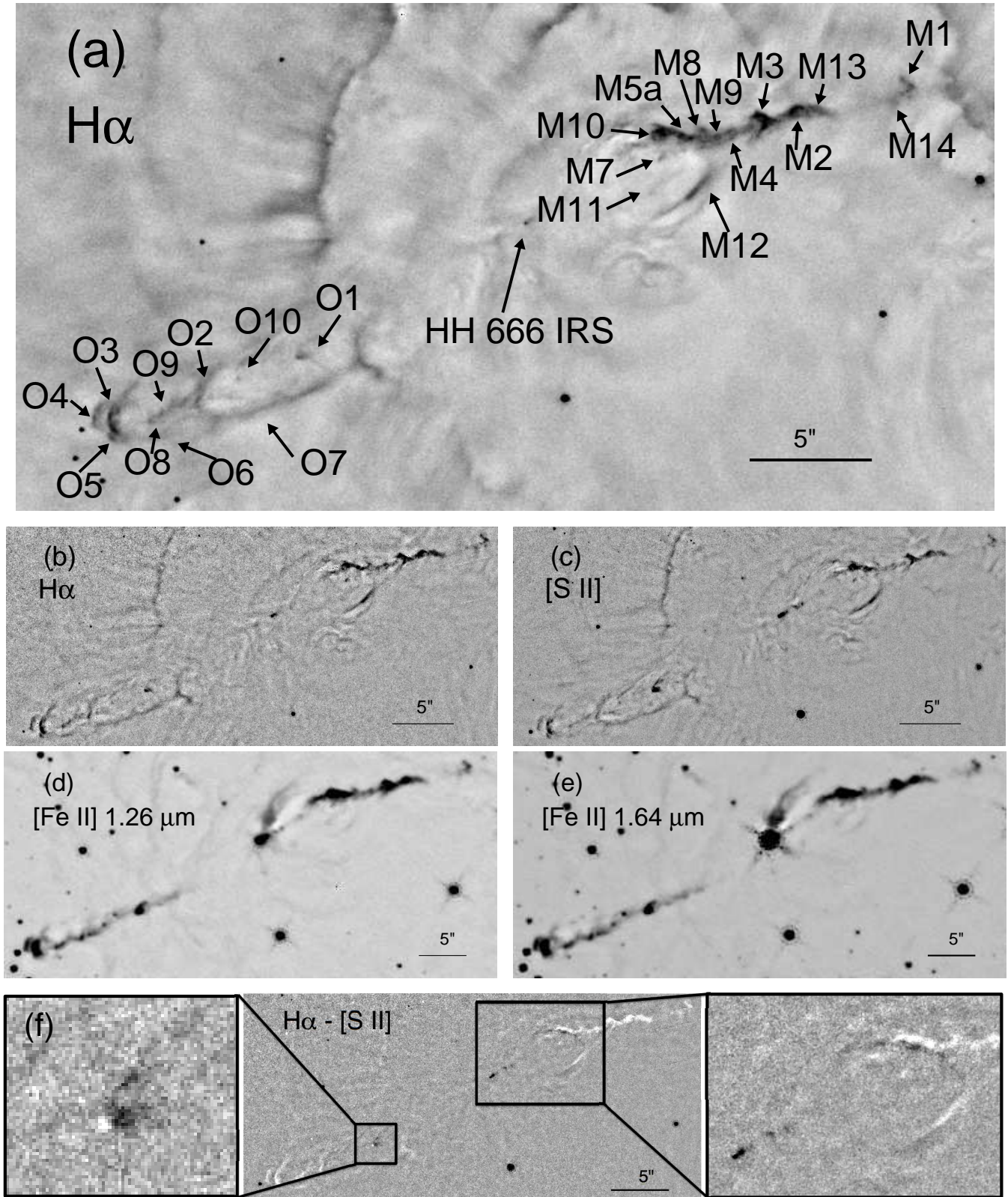
Figure 1. *Top:* New *HST*/ACS Hα image of HH 666 with labels and arrows pointing out features discussed in the text and used to measure proper motions (a). *Middle: HST*/WFC3-UVIS Hα (b) and [S II] (c) images from Reiter & Smith (2013) with an unsharp mask applied to improve the contrast between faint jet features and bright emission from the surface of the dust pillar. Narrowband, near-IR [Fe II] images with an unsharp mask applied to improve contrast are shown in the row below (panels d and e). *Bottom:* An Hα-[S II] difference image (f) showing the offset between the two emission lines (excess Hα emission appears white, [S II] emission is black). Small images on either side show a zoomed-in view of the two places in the innermost jet where the two emission lines are significantly offset.

2   OBSERVATIONS

2.1   Near-IR spectroscopy

Near-IR spectra of HH 666 were obtained with the Folded-Port Infrared Echellette spectrograph (FIRE, Simcoe et al. 2013) on the Baade 6.5-m Magellan telescope on 22 February 2013. Conditions were photometric with thin clouds and the seeing was $\sim 0\rlap{.}''6$. FIRE captures medium resolution spectra from $0.8 - 2.5$ μm simultaneously. The echelle slit is $7''$ long and our data were obtained with a slit width of $0\rlap{.}''6$. This corresponds to a velocity resolution of 50 km s^{-1}. Uncertainties in the measured radial velocities are shown in Figure 3. We used five slit positions to target the brightest [Fe II] emission in the inner $\sim 40''$ of the HH 666 jet and its driving source. Slit positions are shown in Figure 3.

We obtained separate frames offset $\sim 5''$ from the jet axis for the four pointings along HH 666 M and HH 666 O to subtract sky lines and emission from the H II region. For the central slit position that contains the driving source (see Figure 3), we employ an ABBA nod putting the driving source at opposite ends of the slit and remove sky emission by subtracting complementary nods. The total integration time for each slit position is 600 s. The data were reduced using the FIREHOSE IDL pipeline. This data reduction package provides flat-fielding, sky-subtraction, and wavelength calibration of the 2D FIRE spectra. Wavelength calibration was done using a ThAr lamp. We extract the [Fe II] position-velocity diagrams from the reduced, calibrated 2D spectra. The reported velocities are in the heliocentric velocity frame.

2.2   New Hα images

We present new Hα images obtained with *HST*/ACS on 21 February 2014. These images duplicate the observational setup used by Smith et al. (2010) to observe HH 666 on 30 March 2005, providing two epochs with a time baseline of 8.9 yr (see Table 1). Both epochs were observed using the F658N filter (which transmits both Hα and [N II] $\lambda6583$) with a total exposure time of 1000 s. A three-position linear offset pattern was used to fill ACS chip gaps. See Smith et al. (2010) for a more complete description of the observational setup.

By replicating the observational setup of the first-epoch images, we reduce systematic uncertainties in the image registration and measurement of individual blob proper motions. Our image registration procedure is similar to the method described in Anderson et al. (2008a,b), Anderson & van der Marel (2010), and Sohn et al. (2012). This method uses PSF photometry of pipeline-calibrated images that have been bias-subtracted, flat-fielded, and CTE-corrected, but have not been resampled to correct for geometric distortion (denoted with the file extension `flc`). These images are better suited for high-accuracy PSF fitting than drizzled images (denoted by the file extension `drc`), and are therefore preferable to measure precise relative proper motions from *HST* data.

We construct an initial reference frame from the `drc` images using the astrometric information in their headers. Basic centroid positions of bright, relatively-isolated stars in the `drc` images are compiled into a reference frame that has a 50 mas pixel^{-1} scale and is aligned with the y axis pointing north, like that of Anderson et al. (2008a). We then perform PSF photometry on each `flc` exposure using the program `img2xym_WFC.09x10` (Anderson & King 2006), which employs a spatially-variable library of PSFs. Stellar positions are corrected afterward for geometric distortion using the distortion correction from Anderson (2006). Next, six-parameter linear transformations are computed from each distortion-corrected `flc` frame to the initial reference frame via the positions of the stars found in both. For improved accuracy, we recalculate the transformation after replacing the initial reference-frame positions of the stars with their average PSF-based positions transformed from the `flc` frames.

Finally, we construct a stacked image for each epoch by resampling the `flc` images into the reference frame, allowing us to measure the motions of extended sources. The details of the stacking algorithm can be found in Anderson et al. (2008a). As both epochs are transformed to the same reference frame, object positions are directly comparable. The image alignment precision is primarily limited by the internal accuracy of the reference frame and distortion correction (~ 0.015 pixels, see Anderson & King 2006; Sohn et al. 2012), which over our time baseline corresponds to 0.084 mas yr^{-1} or 0.92 km s^{-1} at the distance of Carina (2.3 kpc, Smith 2006b).

To measure proper motions of bright knots in the inner jet, we use our implementation of the modified cross-correlation technique used by Currie et al. (1996, see also Morse et al. 2001, Hartigan et al. 2001, and Reiter & Smith 2014). First, we correct for local diffuse H II region emission by subtracting a median-filtered image from each epoch. Next, we extract bright jet knots using a box size that is optimized for each feature (see Figure 4). To determine the pixel offset between the two epochs, we generate an array that contains the total of the square of the difference between two images for each shift of a small box containing the jet feature relative to a reference image. The best match between the two images will produce the smallest value in the array.

With the identical observational setup and longer time baseline between the two epochs of *HST*/ACS data, we achieve finer velocity resolution than that obtained in our previous study (Reiter & Smith 2014) using *HST*/WFC3-UVIS images taken 4.32 yr after the first-epoch *HST*/ACS images. Using the same camera, filter, and approximate location of the source on the detector (and thus same distortion correction) minimizes systematic uncertainties and allows us to measure proper motions of bright nebular jet features with velocities greater than ~ 10 km s^{-1}. To determine the uncertainty in the pixel offset between the two epochs, we explore the proper motion obtained using different box sizes around each jet feature. We also determine the maximum offset between the two images that still results in good alignment, identified by residuals in a subtraction image on the order of the noise. From this, we determine an average proper motion uncertainty of ~ 10 km s^{-1}, although this depends on the signal-to-noise of the feature (see Table 2).

2.3   Previously published images and spectroscopy

For comparison to the new Hα image and [Fe II] spectra, we include *HST*/WFC3 narrowband Hα, [S II], and [Fe II] 1.26

μm and 1.64 μm images. These were discussed previously by Reiter & Smith (2013). Full observational details can be found in that paper.

We also include the Hα spectrum of HH 666 from Smith et al. (2004). Longslit Hα observations were obtained over a slit length of ∼ 6′. With the cross-dispersing grism and a 1″ slit width, the Hα spectrum has a velocity resolution of ∼ 10 km s^{-1}. More complete details of the observation and reduction are given by Smith et al. (2004).

3 RESULTS

3.1 Morphology in images

High angular resolution images from *HST* reveal the complex morphology of HH 666, particularly in the inner ∼ 40″ of the jet. Hα emission from HH 666 M begins ∼ 10″ to the northwest of the driving source tracing a broad arch around a possible evacuated cavity (see Figure 1) before quickly focusing into a narrow beam. On the opposite side of the driving source (to the southeast), a few Hα-bright knots trace the inner jet. Two bright parabolic arcs with extended wings reach back toward the driving source creating a broad cocoon morphology (features O2 and O3 in Figure 4). Applying an unsharp mask to the Hα image reveals collimated jet emission just inside the terminus of HH 666 O (inside feature O3, see Figures 1 and 4). Comparing Hα and [S II] images from *HST*/WFC3-UVIS demonstrates that the morphology of these two lines is remarkably similar in externally irradiated HH jets (Reiter & Smith 2013). In purely shock-excited gas, however, the location and relative intensity of the two lines will be offset (Hartigan et al. 1994; Heathcote et al. 1996). Thus, in the harsh UV environment of the Carina nebula, photoionization dominates the excitation of the jet, leading to significantly brighter Hα emission compared to [S II], with the typical ratio in HH 666 of [S II]/Hα ∼ 0.03.

There are only two places in the jet where bright [S II] emission diverges from the morphology of the Hα emission (see Figure 1, bottom panel). [S II] emission extends inside the first arc of Hα emission from the jet on either side of HH 666 IRS. To the northwest (HH 666 M), [S II] emission falls just inside the arc of Hα emission that appears to trace a cavity, extending ∼ 0.″25 behind the Hα. On the other side of the driving source in HH 666 O, [S II] is much more pronounced in a difference image, extending nearly 1″ behind the Hα bright knot that marks the emergence of HH 666 O. In a post-shock cooling zone, bright [S II] emission will trail an Hα-bright arc, with the specific geometry depending on the density and ionization fraction of the preshock gas, and the velocity of the shock itself (Hartigan et al. 1994; Heathcote et al. 1996). Such offsets have been observed in high-spatial resolution images of nearby HH jets, and interpreted as spatially resolved post-shock cooling zones (e.g. Heathcote et al. 1996; Reipurth et al. 1997a; Hartigan et al. 2011). Therefore, interpreting HH 666 as a purely photoionized jet would be an oversimplification.

Near-IR [Fe II] emission from HH 666 tells a remarkably different story from that told by the optical emission (Reiter & Smith 2013). A stream of [Fe II] emission in HH 666 M bisects the dark cavity seen in Hα images, connecting the jet to the driving source. Outside the Hα-bright arc bordering the cavity (features M8, M5a, M10,
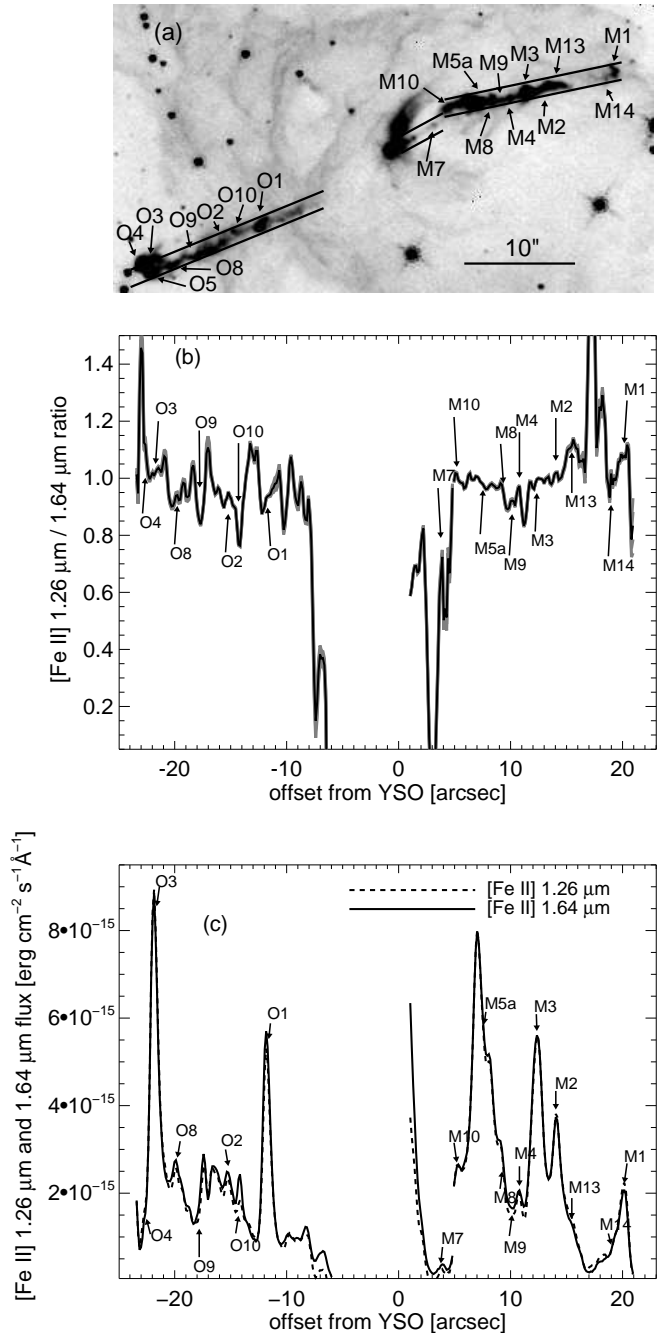

Figure 2. (a) [Fe II] 1.26 μm image of HH 666 with boxes showing the tracing through the jet to measure the [Fe II] ratio $\mathcal{R}$ plotted below. (b) Plot of the [Fe II] 1.26 μm / 1.64 μm ratio $\mathcal{R}$ along the inner jet. The shaded area surrounding the ratio line indicates the standard deviation. (c) Tracing of the [Fe II] 1.26 μm and [Fe II] 1.64 μm flux through the same portions of the inner jet.

M12), [Fe II] emission follows the same morphology as Hα. Morphological discrepancies are even more striking on the opposite side of the jet in HH 666 O. [Fe II] emission does not connect the Hα jet all the way to the driving source, instead beginning ∼ 6″ away from the driving source, closer than the ∼ 11″ offset in the Hα emission. From this point, [Fe II] emission, although clumpy, extends continuously to the bright shock just outside the pillar edge. There is no Hα

or [S II] emission from the collimated jet inside the first Hα arc in HH 666 O (feature O2 in Figure 4). Outside this point, Hα and [S II] emission trace both the cocoon and the jet. Optical emission from the outer jet traces the same morphology as the [Fe II] jet that bisects the larger 'sheath.' Hα, [S II], and [Fe II] emission are all bright at the tip of HH 666 O just outside the edge of the parent pillar (features O9, O8, O3, O4, O5 in Figure 4).

3.2   [Fe II] ratio

We also use the [Fe II] images from Reiter & Smith (2013) to measure the flux ratio of the two observed lines, $\mathcal{R} = \lambda 12567/\lambda 16435$. Both lines originate from the same upper level, so their intrinsic ratio is determined by atomic physics. The observed ratio will decrease as the column of absorbing material increases, so $\mathcal{R}$ provides a measure of the reddening. Smith & Hartigan (2006) measured $\mathcal{R} = 1.49$ in P Cygni while more recent measurements of HH 1 by Giannini et al. (2015) yielded $\mathcal{R} = 1.11 - 1.20$. Since we do not have simultaneous off-line continuum images, we estimate local continuum emission from adjacent regions in the [Fe II] images themselves. We plot $\mathcal{R}$ along the length of the inner jet in Figure 2.

The median flux ratio through the jet is $\mathcal{R} \sim 0.98 \pm 0.15$. This corresponds to an A_V of at least ~ 0.85 mag assuming $\mathcal{R} = 1.49$ and $\sim 0.25 - 0.41$ mag assuming $\mathcal{R} = 1.11 - 1.20$, respectively. Both sides of the jet show an increase in the ratio along the jet moving toward the edge of the pillar. The flux ratio is lowest near the driving source, with a median $\mathcal{R} \sim 0.63$, corresponding to $A_V \gtrsim 1.75$ mag for the Smith & Hartigan (2006) value of $\mathcal{R}$, or $A_V \gtrsim 1.15 - 1.31$ mag using the Giannini et al. (2015) values. In contrast, the ratio is closest to the intrinsic value where we do not observe strong [Fe II] emission from the jet (e.g. outside feature O4 and between features M13 and M14 in Figure 2).

3.3   Velocities from spectra

In the HH 666 discovery paper, Smith et al. (2004) published longslit Hα and [S II] spectra that confirmed that bright knots to the east and west of the dust pillar are part of a coherent bipolar outflow. Doppler velocities in Hα and [S II] spectra show that the western limb of the jet (including HH 666 M) is blueshifted and the eastern limb (HH 666 O) is redshifted, with velocities from the inner jet reaching ± 250 km s^{-1} (Smith et al. 2004). The rapid increase in velocity away from the driving source on both sides of the jet shows an almost Hubble-like velocity structure. In a Hubble flow, velocity is proportional to the distance, $v \propto d$. Smith et al. (2004) derive a "Hubble constant" for HH 666 of $H_{HH\ 666} \simeq 1200(\tan i)$ km s^{-1} pc^{-1}, where i is the inclination for the fast inner jet. A few of the more distant knots in HH 666 also show an increase in velocity with distance from the driving source. Both Hα and [S II] emission traces this velocity structure, mirroring the close match of their morphology in images.

The kinematics traced by [Fe II] emission are as discrepant as the morphology in images. Unlike the Hα kinematics of HH 666, the [Fe II] emission traces steady velocities on either side of the jet. An absence of sharp velocity drops

that suggests that no strong shocks decelerate the jet. Velocities traced by near-IR [Fe II] are ± 200 km s^{-1} throughout the inner jet (see Figure 3).

3.4   New proper motions

We compare new ACS Hα images obtained in 2014 to the first epoch images obtained ~ 9 yrs earlier by Smith et al. (2010) and measure proper motions of jet features. In general, the measured velocities agree with those found by Reiter & Smith (2014) within the uncertainties (see Table 2), although the better match of the instrument and filter used in this work permit higher precision than in our previous work.

With the longer time baseline and better match of the observational setup, we can also measure proper motions of slower features and off-axis motions with greater fidelity. The most remarkable motions we uncover with the latest epoch shows clear *lateral* expansion of the cocoon seen in Hα emission (see Figure 4). In particular, we measure a transverse velocity for feature M12 of 64 km s^{-1} and it appears to move at an angle $\sim 10°$ away from the jet axis defined by the motion of features M8, M5a, M10. Similar lateral expansion in features O6, O7 from HH 666 O traces the slow expansion of the Hα sheath surrounding the [Fe II] jet. A slower velocity and an off-axis propagation direction are predicted for the expanding wings of a bow shock (e.g. Ostriker et al. 2001).

4   RESOLVING MORPHOLOGICAL AND KINEMATIC DISCREPANCIES

Given the striking disparity in the morphology and kinematics traced by Hα and [Fe II] emission in both images and spectra, we propose that these two different emission lines trace physically distinct components of the HH 666 outflow. We illustrate the anatomy of a dense, externally irradiated protostellar outflow in Figure 5, and discuss the evidence for this picture below.

4.1   Redshifted lobe: HH 666 O

In HH 666 O, the redshifted part of the outflow to the southeast of the protostar, Hα emission appears to form a cocoon that surrounds the [Fe II] jet core. The large spatial offset of the Hα emission from the [Fe II] ($\sim 2''$) suggests that it traces an entirely different component of the outflow. In fact, the thin arcuate morphology of the Hα and [S II] emission along the face of the pillar resembles the molecular outflow lobes seen at longer (mm) wavelengths (e.g. HH 211, Gueth & Guilloteau 1999; Dionatos et al. 2010; Tappe et al. 2012). Prompt entrainment of ambient material via bow shocks from episodic jets has been invoked to explain nested outflow shells (e.g. Narayanan & Walker 1996). Jets in Carina that are driven by protostars embedded in a dust pillar (more than half the jets discovered by Smith et al. 2010) will entrain material as they exit the cloud.

Kinematics in the Hα spectrum also support the interpretation that Hα emission traces an externally irradiated outflow shell in HH 666. Fast, ionized material at the head of the bow shock that creates this outflow shell corresponds
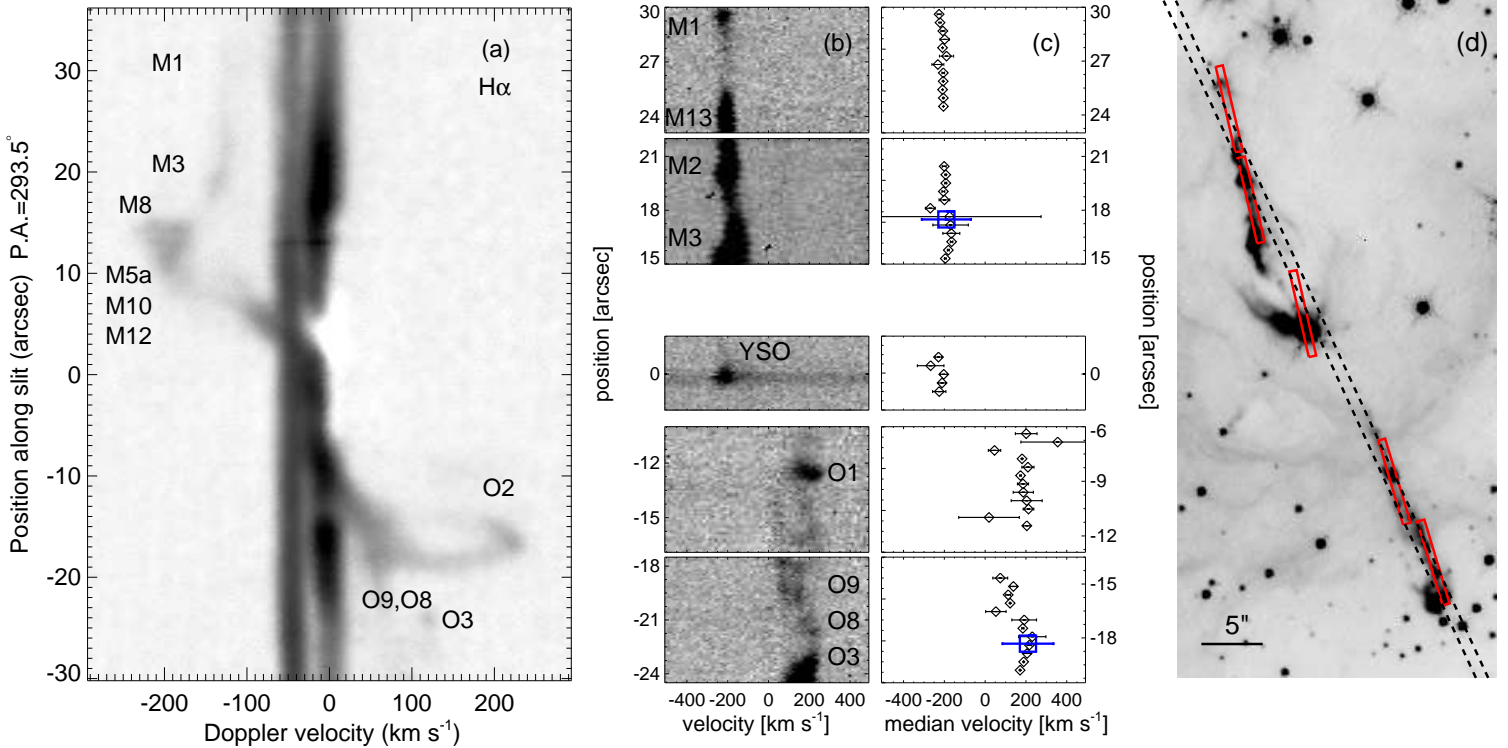
Figure 3. (a) Hα position-velocity diagram of HH 666 from Smith et al. (2004). (b) New, near-IR [Fe II] 1.26 μm spectra obtained with five separate slit positions shown to the right. Alongside the [Fe II] position-velocity diagram, we plot the median line velocity over steps of ∼ 0″6 (c). Blue boxes show the Hα velocities for HH 666 M and O determined by Smith et al. (2004). (d) FIRE slit positions shown as red boxes on a [Fe II] 1.26μm + 1.64 μm image from *HST*/WFC3-IR. The dotted line indicates the slit position used to obtain the longslit Hα spectrum.

to the highest velocities seen in the Hα spectrum. Velocities observed closer to the driving source are lower because they are dominated by emission from the slower wings of the bow shock. The slowest velocities will be observed farthest from the apex of the bow shock, and therefore closest to the driving source (see, e.g. Figure 1 in Arce & Goodman 2002). In this picture, the bow shock dominates entrainment of the ambient gas and will create the observed Hubble-like velocity structure, as seen in the position-velocity diagrams of molecular outflows (e.g. HH 300, Arce & Goodman 2001b). In contrast to the Hα emission, Doppler velocities in the collimated [Fe II] jet are remarkably constant throughout HH 666 O, remaining close to +200 km s^{-1}, as expected for an unimpeded jet propagating away from its driving source. We do not detect evidence for a Hubble-flow in the [Fe II] emission from the jet. If environmental interaction is dominated by the first impulse from the jet, portions of the jet traced by [Fe II] that travel in the wake of the initial bow shock will transfer little momentum to the environment.

Some optical emission from the jet body in the outer portions of HH 666 O, near the leading bow shock (feature O3 in Figure 4, also see Figure 1) further supports the idea that there are two externally irradiated outflow components visible in HH 666. Hα, [S II], and [Fe II] emission begin to coincide just beyond the edge of the dust pillar, marking the first place where the newly liberated *jet* is laid bare to ionizing radiation. Optical emission from the *jet* beyond the pillar edge suggests a decrease in the intervening opti-

cal depth, and the increase of the [Fe II] ratio $\mathcal{R}$ toward the terminus of HH 666 O supports this interpretation. However, the ratio only approaches the intrinsic value beyond the end of the jet, suggesting that the observed reddening is primarily from the jet itself (see Figure 2).

4.2 Blueshifted lobe: HH 666 M

The blueshifted part of the outflow, HH 666 M, that extends to the northwest of the protostar reveals a similar picture to HH 666 O. Close to the driving source (within ≲ 10″), the behavior of the Hα and [Fe II] emission in HH 666 M resembles that of HH 666 O. A narrow column of knotty [Fe II] emission bisects broad, arc-like Hα emission before the morphologies traced by the two lines converge at larger distances from the protostar. New Hα images show that the head of the Hα arc moves along the jet axis while its wings expand laterally away from it. Features M8, M5a, M10 (see Figure 4) move primarily along the jet axis with a transverse velocity of ∼ 150 km s^{-1}. Feature M12 travels at an ∼ 10° angle away from the jet axis, indicating that this emission feature traces the expansion of the Hα arc away from the jet axis. Expanding Hα emission suggests that the arc may be the bow shock where HH 666 M breaks out of the front side of the parent cloud (approximately at the location of feature M9). In this picture, the 'dark patch' to the northwest of the driving source is a cavity cleared by the jet as it plows out of the molecular cloud, leaving a deficit of material behind the

Table 2. Proper motions in the HH 666 inner jet

Object	δx mas	δy mas	v_T[a] [km s^{-1}]	v_R[b] [km s^{-1}]	velocity[c] [km s^{-1}]	α [degrees]	age[d] yr
HH 666 M1	-125 (1)	-34 (1)	159 (4)	-104 (6)	190 (7)	-33 (2)	1108 (34)
HH 666 M14	-122 (3)	-30 (2)	154 (5)	...	161 (5)	...	1097 (42)
HH 666 M13	-122 (1)	-33 (3)	155 (4)	...	162 (4)	...	850 (27)
HH 666 M2	-124 (1)	-40 (1)	159 (4)	...	167 (4)	...	789 (25)
HH 666 M3	-113 (0.5)	-32 (0.2)	143 (3)	-131 (7)	194 (8)	-42 (1)	779 (24)
HH 666 M4	-131 (1)	-25 (2)	163 (4)	...	170 (4)	...	593 (19)
HH 666 M9	-126 (2)	-20 (4)	156 (4)	...	164 (4)	...	568 (19)
HH 666 M8	-123 (1)	-41 (1)	159 (4)	...	166 (4)	...	537 (17)
HH 666 M5a	-117 (1)	-31 (2)	149 (3)	-193 (6)	243 (7)	-52 (1)	576 (18)
HH 666 M10	-114 (2)	-37 (1)	147 (4)	-193 (6)	242 (7)	-53 (1)	472 (16)
HH 666 M7	-124 (1)	-37 (1)	158 (4)	...	166 (4)	...	405 (13)
HH 666 M11	-95 (3)	-19 (3)	118 (5)	...	124 (5)	...	462 (21)
HH 666 M12	-52 (0.1)	-7 (0.3)	64 (1)	...	67 (2)	...	1193 (37)
HH 666 O1	107 (2)	66 (1)	154 (4)	...	162 (4)	...	741 (24)
HH 666 O10	123 (3)	47 (3)	162 (5)	...	169 (6)	...	895 (35)
HH 666 O2	88 (3)	63 (6)	132 (6)	223 (18)	259 (19)	59 (4)	1249 (66)
HH 666 O9	117 (3)	94 (5)	184 (7)	57 (8)	192 (10)	17 (1)	989 (41)
HH 666 O8	134 (2)	67 (2)	184 (5)	57 (8)	192 (9)	17 (0.4)	1017 (34)
HH 666 O3	108 (1)	54 (1)	148 (4)	...	155 (4)	...	1363 (44)
HH 666 O4	91 (1)	59 (2)	133 (3)	121 (4)	180 (5)	42 (1)	1564 (52)
HH 666 O5	108 (2)	47 (2)	144 (4)	...	151 (4)	...	1434 (52)
HH 666 O6	50 (67)	52 (52)	88 (73)	...	92 (77)	...	2156 (1792)
HH 666 O7	9 (3)	35 (2)	45 (3)	...	47 (3)	...	3210 (194)

Uncertainties for each quantity are listed in parenthesis.
[a] The transverse velocity, assuming a distance of 2.3 kpc, measured over $\Delta t = 8.9$ yr.
[b] The radial velocity.
[c] The total space velocity, assuming the average inclination of 42° where the radial velocity could not be matched.
[d] Time for the object to reach its current position at the measured velocity, assuming ballistic motion.

bow shock. Smith et al. (2010) also suggested that a Cantó nozzle (Cantó & Rodriguez 1980; Cantó et al. 1981) may be responsible for refocusing the jet at this point.

Spectra support the interpretation that the Hα arc traces the tip of the expanding outflow cavity. We observe a Hubble wedge in HH 666 M, with Hα emission tracing increasing velocities up until a sharp drop corresponding to features M5a, M10, M12 (see Figure 3). Inside feature M9, closer to the driving source, there is a clear deficit of emission from the globule. However, at the same place along the slit where globule emission decreases, we see blueshifted emission that extends smoothly toward feature M9. Thus, it appears that Hα emission from the inner portion of HH 666 M also traces the expansion of the outflow shell.

A Hubble-like velocity pattern in HH 666 M further suggests that the dark patch to the northwest of the driving source is an evacuated cavity in the dust pillar cleared by the jet. If this is correct, HH 666 O should create a corresponding cavity to the southeast of the driving source as it propagates deeper into the cloud. To test this, we took an intensity tracing through the pillar along the axis of the jet to search for a decrease in the ambient Hα emission on either side of the driving source (see Figure 6). Indeed, intensity tracings reveal dips in the Hα intensity along the pillar extending $\sim 5''$ on either side of the driving source. The emission trough is shallower to the southeast of the driving source, as expected for more foreground emission from the pillar itself.

As in HH 666 O, Doppler velocities measured in the [Fe II] spectra of HH 666 M remain steady, with velocities close to -200 km s^{-1} throughout. Fast, oppositely directed [Fe II] emission is what we expect from a spatially resolved steady *jet*. This structure has been seen in other jets (e.g. Garcia-Lopez et al. 2008; Melnikov et al. 2009; Liu et al. 2012), including those driven by intermediate-mass protostars (e.g. Ellerbroek et al. 2013, 2014). Hubble-like velocities have been observed in protostellar *outflows*, but usually in IR/mm tracers of molecular gas that has been accelerated by an underlying jet (e.g. Arce & Goodman 2001b). Only two other jets show Hubble-like velocities in Hα emission – HH 83 (Reipurth et al. 1989) and HH 900 (Reiter et al. 2015).

Beyond the Hα arc (west of feature M10, outside the globule), Hα and [Fe II] emission converges, thereafter tracing the same morphology. The [Fe II] ratio remains relatively constant (see Figure 2), and velocities traced by both lines remain relatively steady (no strong shocks). Doppler velocities in [Fe II] spectra, however, are nearly 100 km s^{-1} faster than those traced by Hα. Low- and high-velocity components have been observed in jets from low-mass T Tauri stars with velocity differences between the core of the jet and the slightly off-axis wings of as much as ~ 100 km s^{-1} in some cases (e.g. DG Tau, Bacciotti et al. 2000; Pyo et al. 2003). If the shell of material that is traced by Hα inside the globule is pushed back against the jet by feedback from massive stars in the region, then the two components may overlap
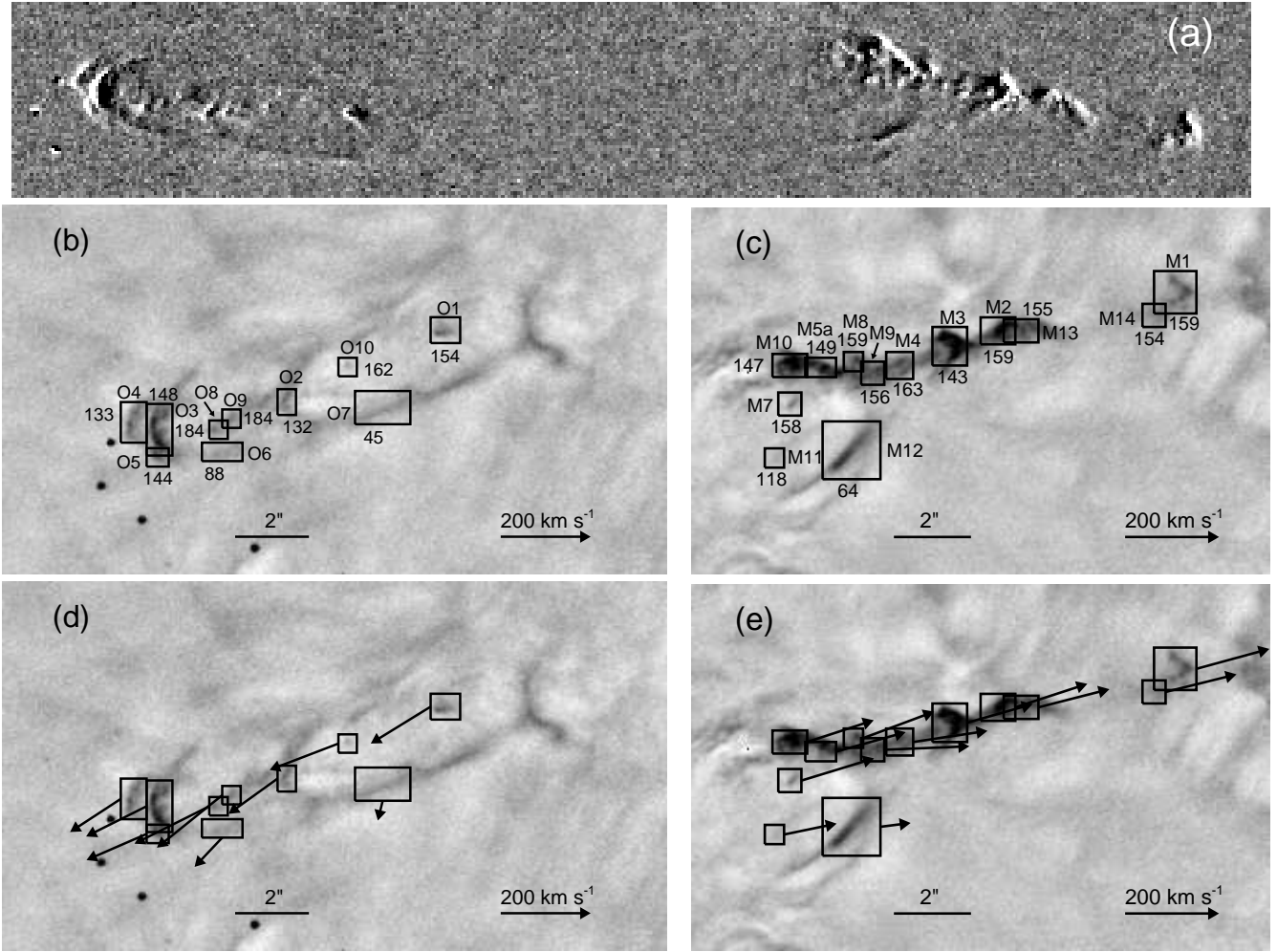
Figure 4. *Top:* Difference image of the first and second epochs of *HST*/ACS imaging (a). *Middle:* New *HST*/ACS Hα image of HH 666 O (b) and HH 666 M (c). Boxes indicate features used to measure proper motions with the name of the feature and the measured transverse velocity labelled alongside. *Bottom:* Same boxes as the middle panel with vectors to indicate the magnitude and direction of the measured motion (d and e).

spatially in images while the entrained material traced by Hα has decelerated as compared to the velocity of the [Fe II] jet.

4.3 An externally irradiated jet and outflow

For embedded jets that entrain an outflow as they plow through a dusty pillar, UV radiation from nearby massive stars will illuminate the shell of the outflow in addition to the jet. We argue that Hα proper motions and Doppler velocities trace the expansion and propagation of the externally irradiated outflow lobe entrained by the jet, but not the jet core. In this picture, we expect larger proper motions from the jet itself (~ 18 mas yr^{-1} for a velocity of 200 km s^{-1}), although additional [Fe II] imaging at a later epoch is required to test this hypothesis.

Our data show that Hα emission traces entrained outflowing gas with the same Hubble-like velocity structure seen in molecular outflows associated with other HH jets (e.g. Lee et al. 2001; Arce & Goodman 2001b). However, the extreme UV radiation in the Carina nebula illuminates en-

trained gas in HH 666, leading to Hα emission from the outflow cocoon. No H_2 emission that is unambiguously associated with the jet has been observed in HH 666 (Smith et al. 2004; Hartigan et al. 2015), although weak H_2 emission will be difficult to discern against the bright background of the photodissociation region (PDR).

5 AN EXPANDING OUTFLOW SHELL FROM AN ONGOING JET BURST

Both morphology and kinematics reveal an Hα outflow lobe encasing the [Fe II] jet to the east and west of the HH 666 driving source. Proper motions reveal the dynamical age of these Hα outflow lobes to be $\sim 1000 - 1500$ yrs (see Table 2). This points to a sudden increase in the jet mass-loss rate ~ 1000 yrs ago that provided a kick to the ambient material now seen as a Hubble flow in Hα emission. Several more distant knots in HH 666 indicate that the jet had other outbursts like this in the past (Smith et al. 2004, 2010).

Steady [Fe II] emission inside the Hα cocoons on either side of the jet indicates that the high-mass-loss rate episode
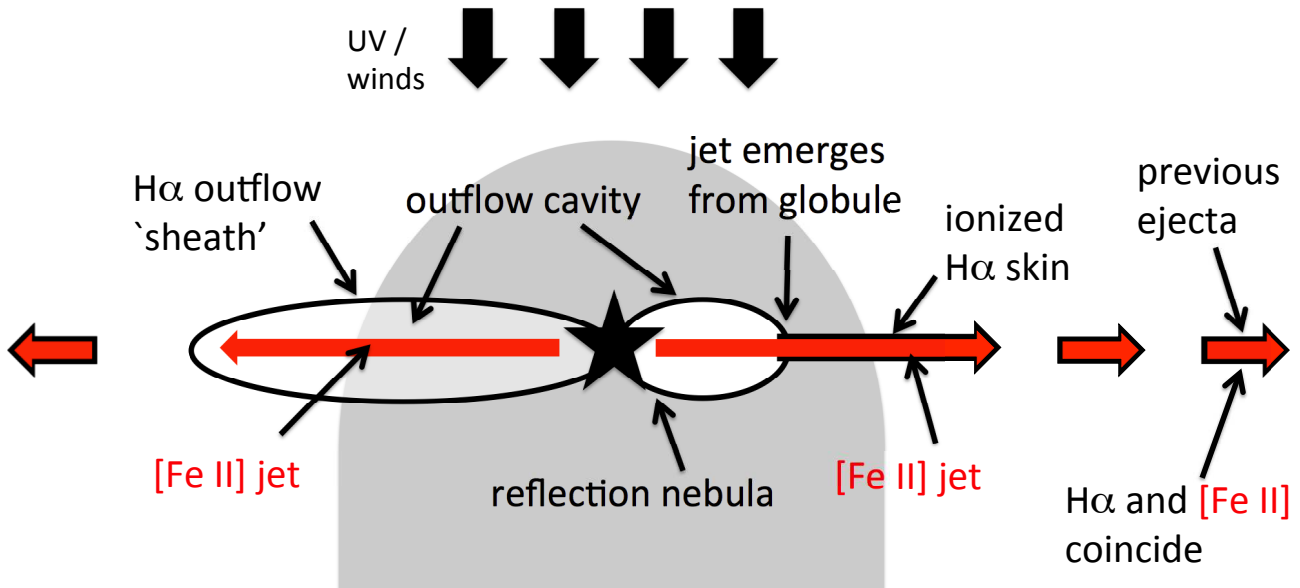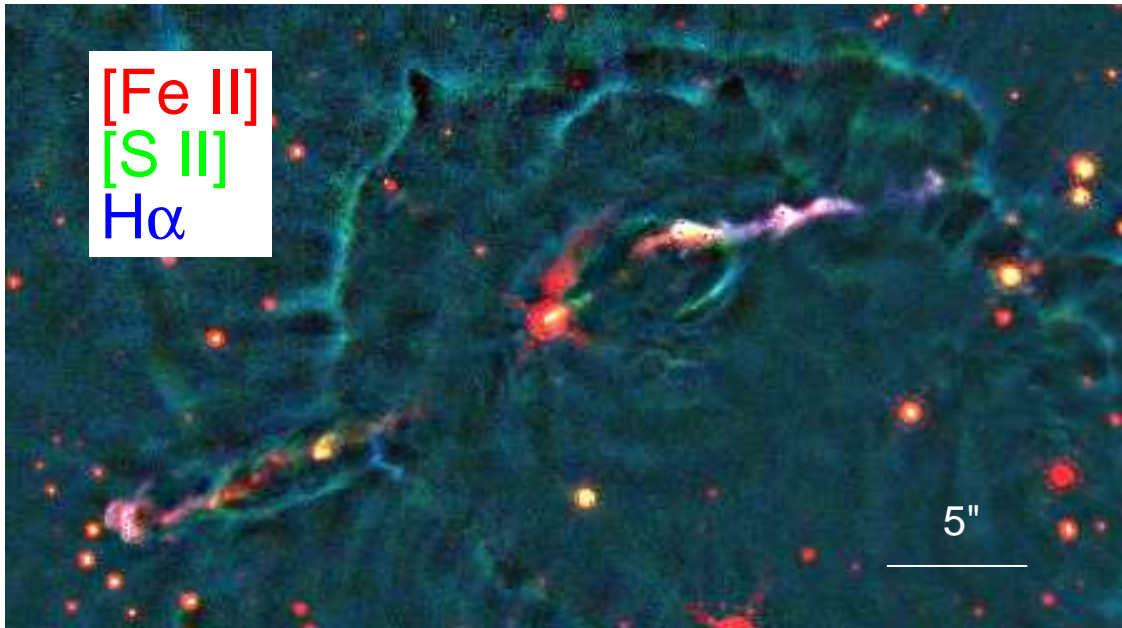
Figure 5. *Top:* Colour image of HH 666 that illustrates the spatial offset between different emission lines in the jet. *Bottom:* Cartoon of the externally irradiated jet and outflow. Red lines show the collimated [Fe II] jet body that clears cavities on either side of the jet. Hα emission, shown in black, traces the ionized edges of these cavities and the ionized skin of the bare jet.

has persisted, with a duration comparable to its age. A burst duration of ~ 1000 yrs is an order of magnitude larger than the estimated decay time of FU Orionis outbursts (e.g. Hartmann & Kenyon 1996). This long duration is on the order of the time between ejections found in HH jets driven by low-mass stars (e.g. Reipurth et al. 1989; Hartigan et al. 1990; Reipurth et al. 1992), and similar to the variability time-scale estimated for HH 46/47 (Raga & Noriega-Crespo 1992). While the burst duration is long compared to those inferred for low-mass protostars, the ~ 1000 yr dynamical time of the inner jet is only a small fraction of the overall age of the HH 666 outflow ($\sim 40,000$ yr, see Reiter & Smith 2014). This points to a strong, sustained increase in the accretion

rate from a relatively evolved intermediate-mass protostar. A larger sample of intermediate-mass protostars is required to determine the frequency and duty cycle of such accretion bursts, and whether they remain stronger than their low-mass counterparts throughout their evolution.

[Fe II] emission from HH 666 traces a steady jet with higher densities and velocities than traced by Hα emission. Reiter & Smith (2013) found that the mass-loss rate implied by the survival of Fe^+ in the jet is an order of magnitude higher than the mass-loss rate derived from the Hα emission measure (Smith et al. 2010). New [Fe II] spectra presented here reveal velocities ± 200 km s^{-1} throughout the inner jet, similar to the fastest velocities in the Hα spec-
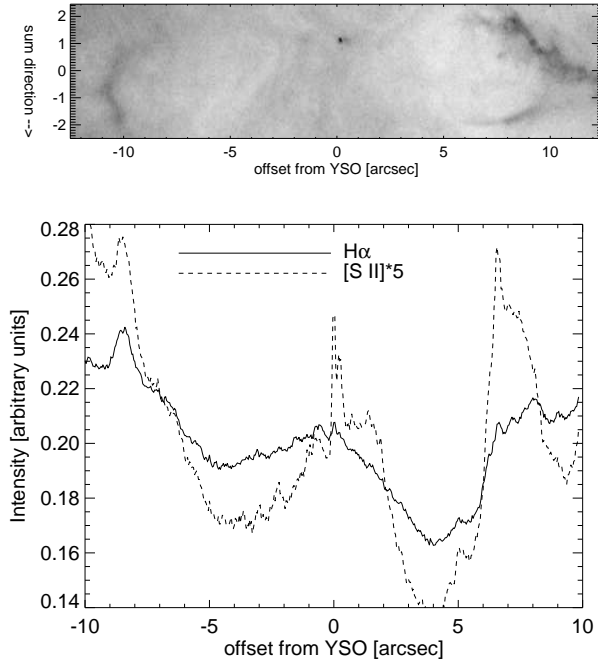
Figure 6. Tracing through the *HST-WFC3* Hα and [S II] images of HH 666. Top panel shows the Hα image of the area used to plot the tracings through the jet environment shown below. The plotted intensity is the total of the emission through the y-direction of the image above (perpendicular to the jet propagation direction). A dark cavity along the northwest limb of the jet is apparent in optical and IR images of the jet. This corresponds to the dip in the flux to the right of the driving source. The dip to the left indicates the presence of a complementary evacuated cavity along the southeast limb of the jet (see Section 4.2).

trum. Applying the median tilt angle of the jet derived from the Hα velocities, $\alpha \approx 42°$ (see Table 2), implies that the three-dimensional velocity of the [Fe II] jet is ~ 300 km s^{-1}, almost twice the speed of the Hα jet. The higher mass-loss rate and velocities in the [Fe II] jet suggest that this component of the outflow has at least an order of magnitude more momentum. However, the steady velocity of the [Fe II] jet traveling in the wake of the initial bow shock suggests little momentum transfer to the local environment. This means that the high momentum of the [Fe II] jet will not be deposited locally in the molecular globule, but rather injected into the H II region where its contribution to driving turbulence in the region will be dwarfed by feedback from massive stars.

6   CONCLUSIONS

In this paper, we propose a solution to the discrepancy observed in the morphology and kinematics of Hα and [Fe II] emission from HH 666, an externally irradiated protostellar outflow in the Carina nebula. Previous high-resolution imaging revealed different morphologies traced by the two lines. We present new, near-IR spectra of the inner jet demonstrating that [Fe II] emission also traces different kinematics. Doppler velocities in the new [Fe II] spectra of the inner jet, features HH 666 M and O, remain remarkably consistent on either side of the jet, tracing velocities of ± 200

km s^{-1} throughout. This stands in stark contrast to the velocity structure seen from the same portions of the jet in the longslit Hα spectrum from Smith et al. (2004). Both HH 666 M and O show Hubble-like velocities in the Hα spectrum with only the fastest Doppler velocities in the Hubble wedges on either side of the driving source approaching the velocities traced by [Fe II].

Hα and [Fe II] emission also trace different morphologies, complementing the velocity discrepancies in spectra (Reiter & Smith 2013). Sheath-like Hα emission encompasses narrow [Fe II] emission on either side of the jet. We argue that broad Hα emission traces the material swept up via prompt entrainment by a jet outburst that began ~ 1000 yrs ago, with bright Hα arcs tracing the head of the bow shock that dominates entrainment. Constant velocity [Fe II] emission, inside the outflow sheath and Hubble flow traced by Hα, indicates that the high-mass-loss rate episode from the jet is ongoing, tracing a strong accretion burst that has been sustained longer than the typical decay time of FU Orionis outbursts. A new epoch of Hα imaging from *HST*/ACS provides a ~ 9 yr time baseline to measure the motion of bright Hα features. Proper motions trace the lateral expansion of the Hα sheath, consistent with an expanding shell around the jet.

We propose that the same underlying physics that drives the molecular outflows seen from more embedded intermediate-mass protostars creates the two-component outflow we observe in HH 666. Unlike jets with molecular outflows, HH 666 resides in a giant H II region, so both the jet and the material it entrains are subject to the harsh UV background created by the many O-type stars in the Carina nebula. This leads to Hα emission from the walls of the outflow cavity and [Fe II] emission from the obscured jet. Outside the parent pillar where a cocoon no longer envelopes the jet, Hα and [Fe II] emission trace the same morphology. Thus, HH 666 provides a missing link that unifies the irradiated outflows driven by unobscured protostars with the molecular outflows typically observed from embedded intermediate-mass protostars.

REFERENCES

Anderson J., 2006, "The 2005 HST calibration workshop: Hubble after the transition to two-gyro mode", Proceedings of a workshop held at the Space Telescope Science

Institute, Baltimore, Maryland, October 26-28, 2005. Eds Koekemoer A.M., Goudfrooij P., Dressel L.L. Greenbelt, MD, 11

Anderson J., King I.R., 2006, "PSFs, Photometry, and Astronomy for the ACS/WFC", 2006, 1

Anderson J., et al., 2008a, AJ, 135, 2055

Anderson J., et al., 2008b, AJ, 135,2114

Anderson J., van der Marel R.P., 2010, ApJ, 710,1032

Arce H.G., Goodman A.A., 2001, ApJ, 554, 132

Arce H.G., Goodman A.A., 2001, ApJL, 551, 171

Arce H.G., Goodman A.A., 2002, ApJ, 575, 928

Arce H.G., Sargent A.I., 2005, ApJ, 624, 232

Arce H.G., Sargent A.I., 2006, ApJ, 646, 1070

Arce H.G., Mardones D., Corder S.A., Garay G., Noriega-Crespo A., Raga A.C., 2013, ApJ, 774, 39

Bacciotti F., Mundt R., Ray T.P., Eislöffel J., Solf J., Camezind M., 2000, ApJ, 537, 49

Bally J., Reipurth B., 2001, ApJ, 546, 299

Bally J., Licht D., Smith N., Walawender J., 2006, AJ, 131, 473

Beltrán M.T., Estalella R., Girart J.M., Ho P.T.P., Anglada G., 2008, A&A, 481, 93

Beuther H., Walsh A.J., Thorwirth S., Zhang Q., Hunter T.R., Megeath S.T., Menten K.M., 2008, A&A, 481, 169

Cantó J., Rodriguez L.F., 1980, ApJ, 239, 982

Cantó J., Rodriguez L.F., Barral J.F., Carral P., 1981, ApJ, 244, 102

Caratti o Garatti A., Froebrich D., Eislöffel J., Giannini T., Nisini B., 2008, A&A, 485, 137

Currie D.G. et al., 1996, AJ, 112, 1115

De Gouveia E.M., Birkinshaw M., Benz W., 1996, ApJL, 460, 111

Dionatos O., Nisini B., Cabrit S., Kristensen L., Pineau des Forêts G., 2010, A&A, 521, 7

Duarte-Cabral A., Bontemps S., Motte F., Hennemann M., Schneider N., André P., 2013, A&A, 558, 125

Ellerbroek L.E., Podio L., Kaper L., Sana H., Huppenkothen D., de Koter A., Monaco L., 2013, A&A, 551, 5

Ellerbroek L.E., et al., 2014, A&A, 563, 87

Forbrich J., Stanke Th., Klein R., Henning Th., Menten K.M., Schreyer K., Posselt B., 2009, A&A, 493, 547

Fuente A. et al., 2009, A&A, 507, 1475

Garay G., Brooks K.J., Mardones D., Norris R.P., 2003, ApJ, 587, 739

Garcia-Lopez R., Nisini B., Giannini T., Eislöffel J., Bacciotti F., Podio L., 2008, A&A, 487, 1019

Giannini, T., et al., 2015, ApJ, 798, 33

Gueth F., Guilloteau S., 1999, A&A, 343, 571

Guzmán A.E., Garay G., Brooks K.J., Voronkov M.A., 2012, ApJ, 753, 51

Hartigan P., Raymond J., Meaburn J., 1990, ApJ, 362, 624

Hartigan P., Morse J.A., Raymond J., 1994, ApJ, 436, 125

Hartigan P., Morse J.A., Reipurth B., Heathcote S., Bally J., 2001, ApJL, 559, 157

Hartigan P., et al., 2011, ApJ, 736, 29

Hartigan P., Reiter M., Smith N., Bally J., 2015, AJ, 149, 101

Hartmann L., Kenyon, S.J., 1996, ARA&A, 34, 207

Heathcote S., Morse J.A., Hartigan P., Reipurth B., Schwartz R.D., Bally J., Stone J.M., 1996, AJ, 112, 1141

Klaassen P.D., et al. 2013, A&A, 555, 73

Lee C.-F., Stone J.M., Ostriker E.C., Mundy L.G., 2001, ApJ, 557, 429

Lefloch B., Cernicharo J., Reipurth B., Pardo J.R., Neri R., 2007, ApJ, 658, 498

Liu C.-F., et al. 2012, ApJ, 749, 62

McGroarty F., Ray T.P., Bally J., 2004, A&A, 415, 189

Melnikov S.Y., Eislöffel J., Bacciotti F., Woitas J., Ray T.P., 2009, A&A, 506, 763

Morse J.A., Kellogg J.R., Bally J., Davidson K., Balick B., Ebbets D., 2001, ApJL, 548, 207

Mundt R., Ray T.P., Raga A.C., 1991, A&A, 252, 740

Nagar N.M., Vogel S.N., Stone J.M., Ostriker E.C., 1997, ApJ, 482, 195

Narayanan G., Walker C.K., 1996, ApJ, 466, 844

Noriega-Crespo A., et al., 2004, ApJS, 154,352

Ostriker E.C., Lee C.-F., Stone J.M., Mundy L.G., 2001, ApJ, 557, 443

Povich M. et al., 2011, ApJS, 194, 14

Pyo T.-S., et al., 2003, ApJ, 590, 340

Raga A.C., Noriega-Crespo A., 1992, Rev. Mex. Astron. Astrofis., 24, 9

Raga A.C., Cabrit S., 1993, A&A, 278, 267

Reipurth B., 1989, A&A, 220, 249

Reipurth B., Raga A.C., Heathcote S., 1992, ApJ, 392, 145

Reipurth B., Hartigan P., Heathcote S., Morse J.A., Bally J., 1997, AJ, 114, 757

Reipurth B., Bally J., Fesen R.A., Devine D., 1998, Nature, 396, 343

Reipurth B., Yu K.C., Heathcote S., Bally J., Rodríguez L.F., 2000, AJ, 120, 1449

Reiter M., Smith, N., 2013, MNRAS, 433, 2226

Reiter M., Smith N., 2014, MNRAS, 445, 3939

Reiter M., Smith N., Kiminki M.M., Bally J., Anderson J. 2015, MNRAS, accepted

Salyk C., Pontoppidan K., Corder S., Muñoz D., Zhang K., Blake G.A., 2014, ApJ, 792, 68

Sepúlveda I., Anglada G., Estalella R., López R., Girart J.M., Yang J., 2011, A&A, 527, 41

Shang H., Allen A., Li Z.-Y., Liu C.-F., Chou M.-Y., Anderson J., 2006, ApJ, 649, 845

Simcoe R.A. et al., 2013, PASP, 125, 270

Smith N., Bally J., Brooks K.J., 2004, AJ, 127, 2793

Smith N., 2006a, MNRAS, 367, 763

Smith N., 2006b, ApJ, 644, 1151

Smith N., Hartigan P., 2006, ApJ, 638, 1045

Smith N., Bally J. Walborn N., 2010, MNRAS, 405, 1153

Sohn S.T., Anderson J., van der Marel R.P., 2012, ApJ, 753, 7

Takahashi S., Ho P.T.P., 2012, ApJ, 745, 10

Tappe A., Forbrich J., Martín S., Yuan Y., Lada C.J., 2012, ApJ, 751, 9

Zapata L.A., Arce H.G., Brassfield E., Palau A., Patel N., Pineda J.E., 2014, MNRAS, 441, 3696

Zinnecker H., McCaughrean M.J., Rayner J.T., 1998, Nature, 394, 862